Multicore iron oxide nanoparticles for magnetic hyperthermia and combination therapy against cancer cells

David García-Soriano, Paula Milán-Rois, Nuria Lafuente-Gómez, Ciro Rodríguez-Díaz, Cristina Navío, Álvaro Somoza and Gorka Salas

Multicore iron oxide nanoparticles for magnetic hyperthermia and combination therapy against cancer cells

David García-Soriano,[1,‡] Paula Milán-Rois,[1,‡] Nuria Lafuente-Gómez[1], Ciro Rodríguez-Díaz[1], Cristina Navío,[1] Álvaro Somoza,[1,2] and Gorka Salas[1,3,].*

[1] Instituto Madrileño de Estudios Avanzados en Nanociencia, Campus Universitario de Cantoblanco, 28049 Madrid, Spain.

[2] Unidad Asociada de Nanobiotecnología (CNB-CSIC e IMDEA Nanociencia), 28049 Madrid, Spain.

[3] Unidad de Nanomateriales Avanzados, IMDEA Nanociencia (Unidad de I+D+I Asociada al Instituto de Ciencia de Materiales de Madrid, CSIC), 28049 Madrid, Spain.

‡ These authors contributed equally to this work.

* Corresponding author: Gorka Salas. Instituto Madrileño de Estudios Avanzados en Nanociencia (IMDEA Nanociencia), Campus Universitario de Cantoblanco, 28049 Madrid, Spain. Phone: +34 912998850; email: gorka.salas@imdea.org

Unidad de Nanomateriales Avanzados, IMDEA Nanociencia (Unidad de I+D+I Asociada al Instituto de Ciencia de Materiales de Madrid, CSIC), 28049 Madrid, Spain.

ABSTRACT

Hypothesis

Multicore flower-like iron oxide nanoparticles (IONPs) are among the best candidates for magnetic hyperthermia applications against cancers. However, they are rarely investigated in physiological environments and their efficacy against cancer cells has been even less studied. The combination of magnetic hyperthermia using multicore IONPs with selected bioactive molecules should lead to an enhanced activity against cancer cells.

Experiments

Multicore IONPs were synthesized by a seeded-growth thermal decomposition approach. Then, the cytotoxicity, cell uptake, and efficacy of the magnetic hyperthermia approach were studied with six cancer cell lines: PANC1 (pancreatic carcinoma), Mel202 (uveal melanoma), MCF7 (breast adenocarcinoma), MB231 (triple-negative breast cancer line), A549 (lung cancer), and HCT116 (colon cancer). Finally, IONPs were modified with a chemotherapeutic drug (SN38) and tumor suppressor microRNAs (miR-34a, miR-182, let-7b, and miR-137), to study their activity against cancer cells with and without combination with magnetic hyperthermia.

Findings

Two different types of multicore IONPs with very good heating abilities under magnetic stimulation have been prepared. Their concentration-dependent cytotoxicity and internalization have been stablished, showing a strong dependence on the cell line and the nanoparticle type. Magnetic hyperthermia causes significant cell death that is dramatically enhanced in combination with the bioactive molecules.

KEYWORDS: magnetic nanoparticles, nanoflowers, hyperthermia, microRNA, combination therapy, cancer cells.

INTRODUCTION

Magnetic nanoparticles based on iron oxides (IONPs) are among the most attractive inorganic nanoparticles for biomedical applications due to their low toxicity and physicochemical properties.[1] As other nanoparticles, they can be used in drug delivery. Unlike other nanoparticles, they can also be used as contrast agents in magnetic resonance imaging (MRI) and heat generators for magnetic hyperthermia. Hyperthermia refers to increasing the temperature of the target tissue to have a therapeutic effect, and it has been chiefly researched for treating solid tumors.[2] Magnetic hyperthermia can do this in a localized way. It requires the presence of magnetic nanoparticles and the application of an alternating magnetic field (AMF) with the appropriate field and frequency.[3] The ability of magnetic nanoparticles to release heat under AMF is usually evaluated through the specific absorption rate (SAR) or specific loss power (SLP) under given conditions.[2] From a material's viewpoint, optimizing the heating efficiency of magnetic nanoparticles (*i.e.* maximizing their SAR values) is usually accomplished by tuning their size and shape. Therefore, the method employed in their preparation is of utmost importance in the field.[4] Among other approaches, the design of multicore nanostructures, frequently referred to as nanoflowers, has attracted special attention in recent years.[5–12] Clustering nanoparticles in a single nanostructure modifies their magnetic properties through cooperative organization. Some of the highest SAR values in magnetic hyperthermia have been reported using nanoflowers.[5,10,11] The synthesis of flower-like magnetic nanoparticles is usually carried out by the polyol route than other methods.[13–15] Thus, Hugounenq *et al*. synthesized magnetic nanoflowers with sizes between 21 and 55 nm, composed of smaller grains with sizes around 11 nm, by alkaline hydrolysis of iron chlorides in a mixture of diethylene glycol and N-methyldiethanolamine at high temperature.[5] This approach provided improved magnetic properties due to exchange coupling interactions in the multicore nanostructures that, as a consequence, displayed

enhanced heating abilities and relaxivities for MRI contrast.[6] Applying an AMF of 29 $kA \cdot m^{-1}$ and 520 kHz to MCF7 tumor cells incubated with the nanoflowers, between 20 % and 60 % of the cells died, depending on the nanoflowers' concentration. Di Corato *et al*. reported that the iron oxide nanoflowers released more heat than nanoparticles with other shapes, structures, and compositions but that the heating ability is seriously reduced in the cellular environment.[16] McKiernan *et al*. prepared pegylated magnetic nanoflowers that displayed excellent colloidal stability and were studied as contrast agents for magnetic resonance imaging *in* vivo.[17] Despite these promising results, little progress has been made concerning efficacy studies of magnetic hyperthermia in cell cultures.[6,16] Most efforts on the topic have been dedicated to improving the magnetic heating abilities by modifying the polyol method to control the size and shape of the nanoflowers by, for example, adding controlled amounts of water,[8] or employing seeded-growth processes.[10] Another classical method for preparing magnetic nanoparticles is thermal decomposition in organic media.[18,19] Thermal decomposition is usually the method of choice when good control of the size and shape, good crystallinity, and magnetic properties are required. It is also a suitable method to avoid aggregation, which is usually desirable when preparing IONPs. However, it is rarely considered when the goal is to intentionally prepare aggregated multicore nanoparticles to engineer their anisotropy and interactions. It has been argued that, so far, the polyol method has demonstrated more versatility for tuning the size of the flower-like particles and the grains composing it in a more extensive range than by thermal decomposition.[14] Still, some reports have described the preparation of multicore magnetic nanoparticles for MRI applications (though not for magnetic hyperthermia). Thus, Hu *et al*. modified the typical thermal decomposition method, with a mixture of benzyl ether and a polyol derivative (HOOC-PEG-COOH, M_n = 600) that provided multi-core flower-like nanoparticles readily dispersible in water.[20] These nanoflowers showed potential as MRI contrast agents. Nikitin *et al*. prepared clusters of iron oxide nanoparticles by thermal decomposition for MRI applications, too.[21] The control of the aggregation was achieved by changing the organic acids used as surfactants. Given the excellent results attained in the past with the thermal

decomposition method for magnetic hyperthermia,[2] it is worth investigating the use of multicore IONPs prepared by this route in cell cultures.

Here, we report the synthesis by thermal decomposition of multicore flower-like magnetic nanoparticles with excellent properties for magnetic hyperthermia. The synthesis method has been previously employed to prepare iron oxide-manganese oxide and iron oxide-cobalt oxide multicore and core-shell nanoparticles, tuning the size and shape with great versatility.[22,23] In this work, we have adapted the method to prepare two types of multicore iron oxide nanostructures with different sizes and shapes. The concentration-dependent toxicities, time-dependent internalizations, and efficacies as magnetic hyperthermia agents have been studied with multiple cancer cell lines: pancreatic carcinoma, uveal melanoma, breast adenocarcinoma, triple-negative breast cancer, lung, and colon cancer. Finally, we have explored the combination of magnetic hyperthermia with chemotherapy and gene therapy based on magnetic nanoparticles functionalized with a chemotherapeutic drug (SN38) and tumor suppressor microRNAs (miRNAs). Non-coding RNAs, like miRNAs, are regulatory molecules that have opened new anti-cancer approaches.[24,25] The strategy explored in this work is based on the introduction of four tumor suppressor miRNAs (miR-34a, miR-182, let-7b, and miR-137), downregulated in cancer cells, in combination with SN38. The combination of these molecules is shown to increase the antitumor response.[26] IONPs help to improve the solubility and stability of the therapeutic molecules, and bring the possibility of enhancing the efficacy through magnetic hyperthermia.

MATERIALS AND METHODS

Materials.

Commercial products iron(III) chloride hexahydrate (> 98 %), iron(III) acetylacetonate ([$Fe(acac)_3$], 97 %), sodium oleate (≥ 82 %, Riedel-de Haën), oleic acid (90 %), 1,2-dodecanediol (97 %), 1-octadecene

(90 %), *meso*-2,3-dimercaptosuccinic acid (DMSA, 98 %), dimethyl sulfoxide (> 99.5 %) and toluene (99.8 %) are purchased from Aldrich without further purification. Ethanol (99 %) and *n*-hexane (99 %) were purchased from Sharlab. Dialysis tubing cellulose membranes were purchased from Sigma and washed prior to use.

Oligonucleotides were purchased from Integrated DNA Technologies (IDT). Solvents and chemical reagents for modified-SN38 were purchased from Merck Life Science, ABCR GmbH, Thermo Fisher Scientific, VWR, and Scharlab.

Dulbecco's Modified Eagle medium (DMEM, low glucose w/o L-glutamine, Biowest), Roswell Park Memorial Institute (RPMI 1640 w/o L-glutamine) medium, McCoy's 5A medium (w/o L-glutamine, Biowest) sterile filtered reagents phosphate buffered saline modified without calcium chloride and without magnesium chloride (PBS 1x, pH 7.4, Biowest), trypsin/EDTA (1x, VWR), penicillin-streptomycin solution (100x, Biowest), fetal bovine serum (FBS, for standard applications, Fisher), L-glutamine (200 mM, Gibco), dimethyl sulfoxide (DMSO, VWR) and resazurin sodium salt (Sigma-Aldrich, BioReagent, suitable for cell culture). Hydrochloric acid ($HCl_{(aq.)}$, ACS reagent, 37 %), sodium hydroxide (NaOH, ACS reagent, ≥ 97 %), potassium permanganate ($KMnO_4$, ACS reagent, ≥ 99 %), ferrozine (3-(2-pyridyl)-5,6-bis(phenyl sulfonic acid)-1,2,4-triazine), neocuproine (2,9-dimethyl(1,10-phenanthroline)), ammonium acetate ($CH_3CO_2NH_4$, ≥ 97 %) and L-ascorbic acid sodium salt (Sigma-Aldrich) were employed.

Characterization.

The particle size and shape were examined by transmission electron microscopy (TEM; 100 kV, JEOL JEM 1010 microscope). Samples were prepared by depositing one drop of a dilute suspension of the sample in *n*-hexane on a carbon-coated copper grid and allowing it to dry at air and at room temperature. Size distributions were obtained through manual analysis of at least 300 nanoparticles per sample using ImageJ software.[27]

The iron concentration was determined by inductively coupled plasma-optical emission spectrometry (ICP-OES, Perkin-Elmer Optima 2100 DV ICP) after digesting the samples in a HCl:HNO_3 3:1 mixture (with ultrasonication for samples in organic solvents). Then, the samples were diluted adding distilled water up to a known volume (typically, 25 μL of a sample were digested and the diluted in a volumetric flask of 25 mL).

The hydrodynamic diameters (D_{hyd}) of samples at pH = 7.4 were measured by dynamic light scattering (DLS) in a Malvern Zetasizer Nano ZS Instrument, using a red laser at 633 nm and an angle of 173° between the sample and the detector).

X-ray diffraction (XRD) patterns were acquired from powder samples (aqueous samples after lyophilization) with a Bruker D8 Advance A25 system coupled with a PSD Lynseye XE detector (using Cu Kα radiation, scan angle 2θ = 10°-80° at a 0.02 scan step and positive discrimination). The crystallite sizes were determined using the Scherrer equation.

X-ray photoelectron spectroscopy (XPS) was carried out under ultra-high vacuum conditions (base pressure of 5 x 10^{-10} mbar) using a monochromatic Al K-alpha line as the exciting photon source ($h\nu$ = 1486.7 eV). The ejected electrons were collected in a hemispherical energy analyzer (SPHERA-U7, analyzer pass energy set to 20 eV for the XPS measurements to have a resolution of 0.6 eV). Due to the insulating character of the samples, a Flood Gun (FG-500, Specs) with low energy electrons of 3 eV and 40 mA was employed to avoid charging effects. The C 1s centered at 284.6 eV was taken as a binding energy reference.

Vibrating sample magnetometry (VSM) was carried out in a MLVSM9 Mag Lab 2 T (Oxford Instrument). Samples were precipitated, dried, weighed and placed in a gelatin capsule. After saturating the samples in a field of 2 T, the sample magnetization (M) *vs.* applied magnetic field (H) curves were acquired at room temperature. Saturation magnetization (M_S) values, in $A \cdot m^2$ per kg of maghemite, were determined with the experimental M(H) values in the high-field range, where the magnetization

increases linearly with 1/H, extrapolating them to infinite field (1/H = 0). The mass of magnetic material was calculated correcting the weight of the sample with the data acquired by TGA analyses.

Thermogravimetric analysis (TGA) was carried out in a TA Instruments TGA 500, with a heating rate of 10 °C·min^{-1}, in air atmosphere from room temperature to 1000 °C. It was used to determine the percentage of inorganic and organic material present in the samples.

The heating abilities of nanoparticles in colloidal aqueous suspension were measured using a commercial AC field applicator DM100 (nanoscale Biomagnetics). Operating at a field (H_{AC}) of 23.8 kA·m^{-1} and a frequency (f) of 202 kHz. Experiments were carried out within a thermally insulated working space of about 1 cm^3, using a closed container of 1 mL volume conditioned for measurements in the liquid phase. The temperature of the colloids was measured using an optic fiber sensor incorporated in the equipment and registered using a computer. The sample temperature was recorded before applied the magnetic field for 50 seconds to ensure thermal stability. When the field was turned on, the temperature increase was measured for 300 seconds. By performing a linear fit of the data, the slope ($\Delta T \cdot \Delta t^{-1}$) was obtained from 15 to 45 seconds. Measurements started at 35 ºC and the specific absorption rates (SAR) in W/g_{Fe} were obtained from the initial slopes of the temperature *versus* time curves, using the equation $SAR = C_{water}/C_{Fe} * \Delta T/\Delta t$ (where specific heat of water C_{water} = 4.185 J g_{H2O}^{-1} K^{-1}, C_{Fe} is the iron concentration in $g_{Fe} \cdot g_{H2O}^{-1}$, and $\Delta T/\Delta t$ is the slope of the curve).

Synthesis and functionalization of nanoparticles.

Synthesis of iron oxide seeds of 7 nm.[28] Iron(III) acetylacetonate (1.766 g, 5 mmol) was mixed with 1,2-dodecanediol (2.025 g, 10 mmol), oleic acid (4.237 g, 15 mmol.) in 1-octadecene (50 mL) in a three-neck round-bottomed flask with mechanical stirring under a N2 flow at atmospheric pressure. It was heated at a constant rate of 2 ºC·min^{-1} until the temperature reached 100 ºC. After 1 hour, the N_2 flow was stopped and the temperature increased up to 200 ºC at the same rate of 2 ºC·min^{-1}. The mixture was kept at that temperature for 60 minutes. Finally, the temperature was increased again (5

ºC·min^{-1}) to reflux (*ca.* 320 ºC). After 2 hours, the reaction was stopped and allowed to cool down to room temperature. The mixture was washed several times by centrifugation with ethanol (9000 rpm) and redispersed in n-hexane for long-term storage.

Synthesis of iron oxide seeds of 11 nm. Iron(III) acetylacetonate (1.766 g, 5 mmol) was mixed with 1,2-dodecanediol (5.058 g, 25 mmol), oleic acid (4.237 g, 15 mmol.) and oleylamine (4.012 g, 15 mmol) in 1-octadecene (50 mL) in a three-neck round-bottomed flask with mechanical stirring under a N_2 flow at atmospheric pressure. It was heated at a constant rate of 2 ºC·min^{-1} until the temperature reached 100 ºC. After 1 hour, the N_2 flow was stopped and the temperature increased up to 200 ºC at the same rate of 2 ºC·min^{-1}. The mixture was kept at that temperature for 60 minutes. Finally, the temperature was increased again (5 ºC·min^{-1}) to reflux (*ca.* 320 ºC). After 1 hour, the reaction was stopped and allowed to cool down to room temperature. The mixture was washed several times by centrifugation with ethanol (9000 rpm) and redispersed in *n*-hexane for long-term storage.

Prior to their use in the seeded-growth step, the seeds are precipitated again with ethanol and centrifuging, the liquid discarded, the nanoparticles allowed to dry at air, and redispersed in the smallest possible volume of 1-octadecene. The iron concentration was measured by ICP-OES.

Synthesis of NC56 sample. [Fe(acac)$_3$] (1.766 g, 5 mmol) was mixed with oleic acid (4.237 g, 15 mmol) and a suspension of the 7 nm iron oxide seeds (75 mg of Fe) in 1-octadecene (total volume = 50 mL), in a three-neck round-bottomed flask. The mixture was heated up to 60 ºC under a N_2 flow at a constant heating rate of 2 ºC·min^{-1}. After 30 minutes, the N_2 flow was stopped and the mixture heated up again until reflux (*ca.* 320 ºC), at a constant temperature rate of 20 ºC·min^{-1}. After 30 minutes, the heating mantle was switched off and removed, and the dispersion allowed to cool down to room temperature. The mixture was washed several times by centrifugation with ethanol discarding the colourless supernatant with the aid of a magnet. The precipitate was redispersed in the minimum volume possible of *n*-hexane.

Synthesis of NC23 sample. The synthesis procedure was the same as for NC56 but with the seeds of 11 nm (118 mg of Fe).

Surface modification with meso-2,3-dimercaptosuccininc acid (DMSA). NC56 and NC23 nanoparticles were transfer to aqueous dispersion by a ligand substitution process with DMSA as previously described.[29]

IONPs functionalization with SN38. A previously described procedure was employed, with slight modifications.[30] DMSA-coated IONPs were diluted at 2 mg Fe/mL in ultrapure water (1 mL). For acids activation, 2.5 µL of EDC 120 mM (Sigma Aldrich) and 2.5 µL of NHS 60 mM (Sigma Aldrich) in water was added to nanoparticles. The samples were stirred and a mixture of 2.5 µl of cysteamine hydrochloride 40 mM and 2.5 µL of NaOH 40 mM was added. It was incubated in continuous stirring for 16 h at room temperature. Then, nanoparticles were washed 3 times by cycles of centrifugation (16100 rcf, 60 min) and redispersion in ultrapure water. 5 µM final concentration SN38-Pyr was added to the activated nanoparticles. Samples were incubated 16 h under continuous stirring. After that, nanoparticles were washed 3 times (16000 rcf, 60 min). To know the amount of attached SN38, the supernatant was collected to measure 2-pyridinethione (λ_{max} 343 nm, ε_{343nm}= 8080 $L \cdot mol^{-1} \cdot cm^{-1}$) in a microplate reader Synergy H4 hybrid (Agilent BioTek). Finally, functionalized nanoparticles were redispersed in 1 mL ultrapure water.

IONPs functionalization with oligonucleotides.[25] IONPs were modified with thiol groups as previously indicated (2.5 µL of EDC 120 mM, 2.5 µL of NHS 60 mM, 2.5 µL of cysteamine hydrochloride 40 mM, 2.5 µL 40 mM NaOH). Next, 100 µL of aldrithiol 500 µM in DMF (2,2′-dipyridyl disulfide, Sigma Aldrich) were added and incubated under stirring for 16 h. During nanoparticles activation 2-pyridinethione (Pyr) was released to the supernatant. After last incubation, nanoparticles were centrifuged as in the previous step, and the supernatant was measured to quantify the Pyr released (ε_{343nm}= 8080 $L \cdot mol^{-1} \cdot cm^{-1}$) to confirm the correct functionalyzation with Pyr groups

in IONPs surface. Then, 20 μM oligonucleotides (miR mix) with thiol linker (see supporting information) were deprotected by treating 100x excess with 0.5 M tris(2-carboxyethyl)phosphine hydrochloride (TCEP) solution (Sigma Aldrich) for 2 h at room temperature. Then, to remove TCEP excess, NAP-5 column (GE Healthcare) was employed according to manufacturer's indications. The purified oligonucleotide was added to nanoparticles and stirred for 16 h at room temperature. Finally, the dispersion of nanoparticles was washed by centrifugation (12000 rcf, 20 min) and the released Pyr was quantified to know the amount of oligonucleotide attached to the nanoparticles. Nanoparticles were redispersed in 1 mL ultrapure water by stirring with a vortex or pipetting**.**

Cell culture experiments.

The cell lines employed in this article were pancreatic cancer cells PANC1 (ATCC® CRL-1469™) cultured with DMEM low glucose; breast cancer cells MCF7 (ATCC® HTB-22™) cultured with DMEM low glucose; uveal melanoma cells Mel202 (borrowed by Dr. Susana Ortiz Urda, UCSF) cultured with RPMI; triple negative breast cancer cells MB231 (ATCC® HTB-26™), colon cancer cells HTC116 (kindly provided by Dr. Ana Pizarro, IMDEA Nanociencia) cultured with McCoy 5A; and lung cancer A549 cell line (kindly provided by Dr. José Yuste, ISCIII) cultured in RPMI. All the cell culture mediums were supplemented with 10 % FBS, 1 % streptomycin–penicillin and 1 % L-glutamine to obtain complete medium. All the cell cultures were incubated at 37 ˚C in a Binder CB210 incubator (5 % CO_2). All the procedures were performed inside a laminar flow hood Bio II Advance Plus (Telstar).

All the cells, except HCT116, were grown in 96-well plates (10000 cells/well), 24-well plates (60000 cells/well), 6-well plates (180000 cells/well). HCT116 were grown in 5000 cells/well, 30000 cells/well, and 90000 cells/well, respectively.

In all the experiments, the cells were seeded for 24 hours in multi-well plates (according to each experiment). When cells reached 60 % of confluency, they were treated with the corresponding

concentration of IONPs (0.05 mg_{Fe}/mL) for 24 h. In the combined therapy of NC23-miRmix and NC23-SN38 with hyperthermia the used concentrations were 0.01 mg_{Fe}/mL (which corresponds to 100 nM miRmix) and 0.01 mg_{Fe}/mL (corresponding to 25 nM SN38), respectively. The final iron concentration of 0.05 mg_{Fe}/mL was completed adding the non-functionalized NC23 sample.

After 24 h of incubation, the cells were washed with PBS 1x to remove any free nanoparticles and complete fresh medium was added. Then, the following assays were performed.

Cell viability assays. The toxicity of the nanoparticles at different concentrations was studied using the viability assay based on resarzurin salt. Cell viability studies were performed 72 h after treatment with IONPs. A stock solution of resazurin sodium salt (1 $mg \cdot mL^{-1}$) in PBS 1x was diluted to 1 % (*v/v*) in complete medium and was added to the multiwell. After 3 hours of incubation in the incubator, the fluorescence was measured at 25 ˚C in a plate reader Synergy H4 Hybrid reader (BioTEK), λ_{ex} = 550 nm, λ_{em} = 590 nm, gain 50. The fluorescent intensity measurements were processed using the following equation:

$$\%\ Cell\ viability = \left[\frac{(sample\ data - \ negative\ control)}{(positive\ control - negative\ control}\right] \times 100$$

Untreated cells were used as the positive control and resazurin solution without cells was used as the negative control.

Data was represented with Prism GraphPad.

Colorimetric ferrozine-based assay. Cellular uptake experiments were carried out in 6-well plates where the cells were incubated with IONPs during several times. The quantification of the total iron was determined through a ferrozine method, as previously described,[31,32] after different incubation times: 2, 4, 8, 24, 48, and 72 hours. Cells were incubated at 0.05 $mg_{Fe} \cdot mL^{-1}$ and each incubation time corresponds to a single experiment, after which the cells were trypsinized and washed with PBS 1x. Then, the suspension was centrifuged for 5 minutes at 1000 rpm, obtaining a supernatant that was

discarded, and the pellet with the cells was subjected to acid digestion and the ferrozine test. Freshly iron-releasing agent (I.R.A.) was prepared by a 1:1 mixture of 4.5 % $KMnO_4$ in water with 1.4 M HCl. A mixture of 1 M ascorbate, 6.5 M neocuproine, 2.5 M ammonium acetate and 6.5 M ferrozine in water was prepared to obtain the iron detection reagent (I.D.R.). In a typical example, 20 µL of the pellet of cells were dissolved in 80 µL NaOH 50 mM and 100 µL of HCl 10 mM. A volume of 100 µL of the I.R.A. was added into the cell suspension and allow reacting for 3 hours in a thermoblock at 65 ˚C to obtain a blue color dispersion. Then, 30 µL of the I.D.R. mixture was added to each well for the estimation of the total iron content in cells by measuring the absorbance at 565 nm.

TEM micrographs of tumor cells. Cellular morphology and nanoparticle distribution along the cells were examined by transmission electron microscopy (TEM). Cells were seeded in 6-well plate and then treated with IONPs. After 24h the cells were washed with PBS 1x and trypsinized with 200 µl trypsin/EDTA 1x. Tripsinization was stopped with 400 µl complete medium and then cells were centrifuged for 5 min 177 rcf for 5 min in an Eppendorf centrifuge 5804 R. The medium was discarded ant 500 µl PBS 1x medium was added. Next, another 5 min centrifugation step was performed and after that PBS 1x was discarded and the cells were fixed with a mixture of 2 % paraformaldehyde (Polysciences Inc.) and 2.5 % glutaraldehyde (TAAB Laboratories) in PBS 1x for 1 hour at RT. The cells were washed with PBS 1x and then with distilled water, post-fixed (45 minutes) with 1 % osmium tetroxide in PBS 1x (TAAB Laboratories), washed with distilled water, treated (45 minutes) with 1 % aqueous uranyl acetate (Electron Microscopy Sciences), dehydrated with increasing concentrations of ethanol (SeccoSolv; Merck) and embedded in epoxy resin EML812 (TAAB Laboratories; 2 days, room temperature). Resin-containing gelatin capsules (TAAB) were placed on coverslips and polymerized (2 days, 60 ˚C). Resin blocks were detached from coverslips by successive immersion in liquid nitrogen and hot water. Ultrathin 70 nm-thick sections were obtained with an Ultracut UCT ultramicrotome (Leica Microsystems), transferred to 200 mesh nickel TEM grids (Gilder) and stained with 3 %

aqueous uranyl acetate (20 minutes) and lead citrate (2 minutes). Finally, microphotographs were done with a JEOL JEM 1010 microscope (operating at 80 kV), at Servicio Interdepartamental de Investigación of Universidad Autónoma de Madrid.

Magnetic hyperthermia treatment in cell cultures. 8000 cells per well were seeded inside silicone insert 4-wells for self-insertion (Ibidi) which were fixed to 35 mm dishes (VWR) with poly-L-lysine (Thermo fisher). For each condition, two dishes of 35 mm were used, meaning eight wells. Cells were treated with IONPs for 24 h and then the wells were introduced in pairs in a DM100 magnetometer (Nanoscale Biomagnetics). In the combination experiments, all the conditions were treated with the same final NC23 concentration (0.05 mg_{Fe}/mL) by mixing the proper therapeutic nanoparticle with non-functionalized nanoparticles. AMF was applied for 20 min, 202 mHz and 23.8 $kA \cdot m^{-1}$. Then, cells were washed with PBS 1x and cell viability assay was done at 0h, 24h, 48h and 72h after AMF application.

Statistical analysis. Statistical analysis and graphical representations were performed using GraphPad Prism (GraphPad Software), Microsoft Excel (Office 365) and R Project for Statistical Computing (R-3.2.5) software (R Development Core Team, Vienna, Austria). One-way analysis of variance (ANOVA) was used to compare the mean value of each condition *versus* control. The threshold for significance were $P = 0.05$ and $P < 0.05$ (*), $P < 0.01$ (**), $P < 0.001$ (***), and non-significant (ns).

RESULTS AND DISCUSSION

Iron oxide multicore nanoparticles were synthesized by a two-step seeded-growth procedure.[18] Two different seed's sizes were employed for the growth step. Firstly, iron oxide nanoparticles (IONPs) with mean sizes of 7 and 11 nm, narrow size distributions, and spherical shapes (Figure 1), were synthesized by thermal decomposition of iron precursors in 1-octadecene. For the second step, iron(iii) acetylacetonate ($[Fe(acac)_3]$) was mixed with oleic acid and decomposed in the presence of the previously synthesized IONPs, adapting a procedure previously developed by our group to grow

manganese oxide and cobalt oxide shells on IONPs.[22,23] The concentration of [Fe(acac)$_3$] (0.1 M) and oleic acid (0.3 M) was the same independently of the seeds' size used. On the other hand, the concentration of the seeds was adjusted in order to keep constant the total exposed surface area (where the growth of iron oxide occurs). Thus, 75 mg of iron (27 mM) were employed when the 7 nm IONPs were used as seeds, and 118 mg (42 mM) in the case of the 11 nm IONPs. In both cases, the total surface area exposed by the seeds is $1.88 \cdot 10^{22}$ nm^2 (or 18800 m^2), considering them as spherical-shaped nanoparticles (see Experimental section and Table S1 for details).[33] After the seeded-growth process, the 7 nm seeds gave rise to flower-like nanoclusters of 56 nm formed by smaller nanoparticles of around 9 nm tightly joined (Figure 1).

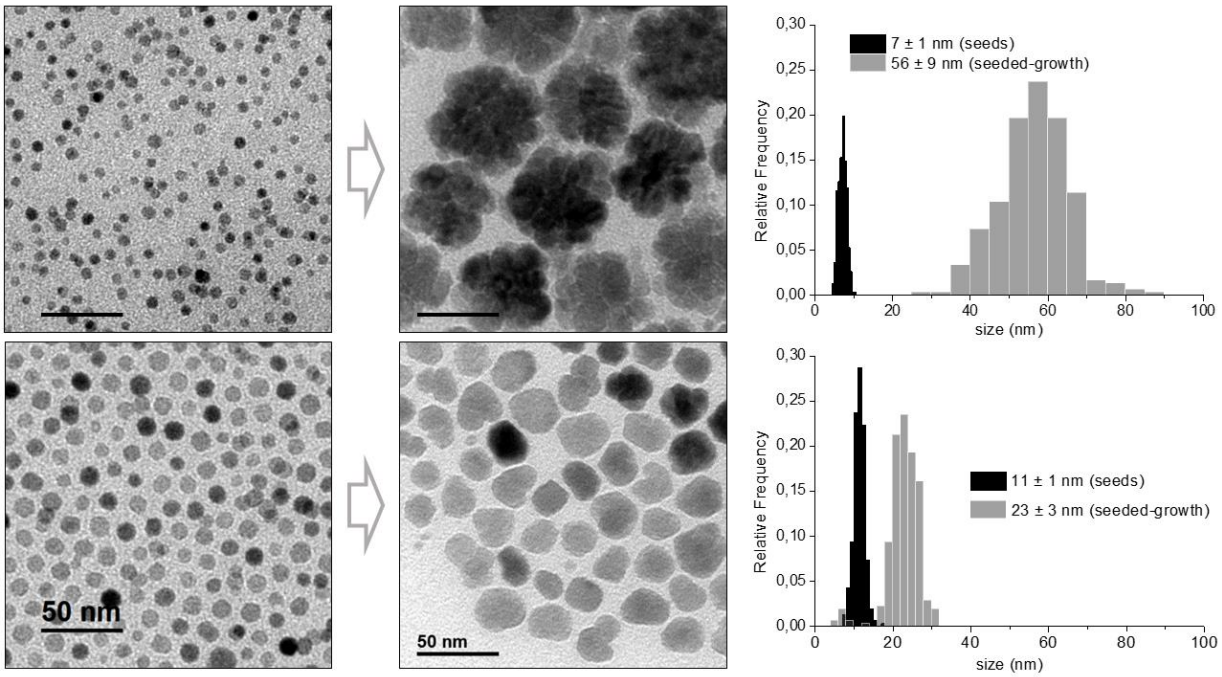

Figure 1. Top row: TEM micrographs of the 7 nm iron oxide nanoparticles (left), multicore nanoflowers (middle) obtained from them, and the corresponding size histograms before and after the seeded growth process (right). Bottom row: TEM micrographs of the 11 nm iron oxide nanoparticles (left), multicore anisotropic nanoparticles (middle) obtained from them, and size histograms before and after the seeded growth process (right).

The nanoclusters' shape resembles that of the previously reported iron oxide nanoflowers prepared by the polyol method.[5,6] By contrast, when the 11 nm IONPs were used as seeds, anisotropic nanoclusters of 23 nm (Figure 1) were obtained. Their shape resembled irregular polygons, with most anisotropic nanostructures apparently formed by 2-3 smaller nanoparticles. Remarkably, very similar results were obtained when the same procedure was applied with independently prepared IONP seeds of 10 nm. In this case, irregular polygons of 24 nm were obtained (Figure S1). The hydrophobic nanoflowers and irregular nanopolygons (termed NC56 and NC23 from now on) were transferred to aqueous dispersion through a ligand substitution process with *meso*-2,3-dimercaptosuccinic acid (DMSA).[34]

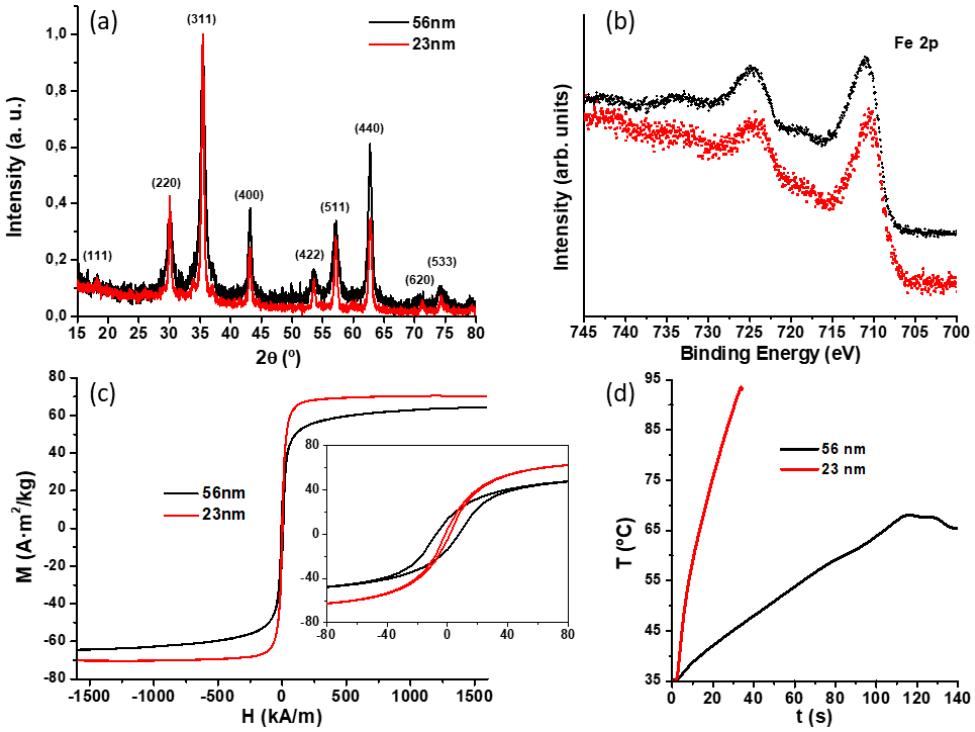

Figure 2. (a) X-ray diffractograms of the multicore nanoparticles NC56 (black line) and NC23 (red line) obtained from the 7 and 11 nm cores, respectively. Main peaks assigned by comparison with γ-Fe_3O_4 JCPDS card-39-1346. (b) XPS curves for Fe 2p signals in NC56 (black line) and NC23 (red line). (c) Magnetization (M) against applied magnetic field (H) curves for NC23 and NC56 at room temperature. Inset: low-field regime M(H) loops. (d) Experimental heating curves for the DMSA-coated NC56 (black) and NC23 (red) at [Fe] = 4 mg·mL^{-1} under an alternating magnetic field of 23.8 kA·m^{-1} and 202 kHz.

In XPS analyses, the chemical state observed in both cases in the Fe 2p core level was Fe^{3+}, as it corresponds to a maghemite phase, which is consistent with the results obtained from XRD analyses (Figure 2). The crystallite sizes calculated through the Scherrer equation, were 8.9 nm and 11.9 nm for the 56 nm nanoflowers and 23 nm nanopolygons, respectively (Table 1). This supports the observation done by TEM of the seeded-growth nanostructures being nanoclusters formed by smaller nanoparticles or grains that are strongly bound within each nanostructure.

Sample	**D_{TEM} ± s.d. (nm)**	**D_{XRD} (nm)**	**D_{hyd}, PdI (nm) H_2O**	**D_{hyd} , PdI (nm) DMEM+FBS**	**D_{hyd} , PdI (nm) RPMI+FBS**	**M_S ($A \cdot m^2/kg$)**	**H_C (kA/m)**	**SAR (W/g_{Fe})**
NC56	56 ± 9	8.9	90, 0.15	176, 0.15	174, 0.15	64	7.6	305
NC23	23 ± 3	11.9	43, 0.19	200, 0.23	114, 0.19	70	1.6	1540

Table 1. Characterization data for the NC56 and NC23 samples. Diameter measured by TEM (D_{TEM}) and estimated by XRD (D_{XRD}). Hydrodynamic diameter (D_{hyd}) and polydispersity index (PdI) in aqueous dispersion (water, DMEM+FBS, RPMI+FBS) measured by DLS. Saturation magnetization (M_S) and coercive field (H_C) determined by VSM. Specific absorption rates (SAR) measured applying an alternating magnetic field of 23.8 $kA \cdot m^{-1}$ and 202 kHz to suspensions of the samples in water (4 mg_{Fe}/mL).

The field-dependent magnetizations of the nanoclusters were measured by VSM. The saturation magnetization (M_S) values of NC23 and NC56 samples were 70 and 64 $A \cdot m^2/kg$, respectively, typical of bulk maghemite at room temperature.[35] Both samples exhibit ferrimagnetic behaviour (Figure 2) featuring very small coercive (H_C) field values (Table 1), with NC23 below the value range reported for bulk maghemite and NC56 close to its lower limit.[36] Noteworthy, nanoflowers prepared by the polyol method are commonly reported to display no or negligible coercivity.[37] Nevertheless, the blocking temperature increases with the size of the multicore nanoparticles probably due to magnetic interactions between neighbouring nanocrystals within the multicore aggregate.[11,38] This seems to apply also in our case, especially in the larger nanoflowers NC56 where the magnetic coupling of

tightly bound superparamagnetic nanoparticles give rise to a net magnetic moment at room temperature. Previous reports have demonstrated that it is possible to prepare stable colloids with ferrimagnetic nanocubes and ferromagnetic Fe/Fe oxide nanoparticles (H_C up to 29.4 kA/m), using appropriate surface stabilizers, and use them *in vivo* as contrast agents in magnetic resonance imaging.[39,40] The DMSA-coated NC56 and NC23 nanoparticles give rise to stable dispersions in water with hydrodynamic diameters (D_{hyd}) of 90 nm and 43 nm (Table 1 and Figure S2), respectively. These values are very close to the TEM sizes, indicating that there is almost no aggregation between the nanoclusters.[41] In DMEM and RPMI supplemented with 10 % FBS (the media used for the cell cultures), D_{hyd} values increased compared to pure water, as expected due to some degree of aggregation and protein adherence to the nanoclusters.[42] Notwithstanding the increase in size, the D_{hyd} values in cell culture media were relatively small ($\leq$ 200 nm, Table 1), taking into account the initial values. It is important to note that the suspensions remain stable at room temperature with no sign of precipitation.

To compare the heating abilities of the nanoparticles, the specific absorption rates (SAR) were calculated from the temperature increase with time when an alternating magnetic field (AMF) of 23.8 $kA \cdot m^{-1}$ and 202 kHz was applied (Figure 2, Table 1). The SAR values measured for NC56 and NC23 nanoparticles in water, at an iron concentration of 4 $mg \cdot mL^{-1}$, were 305 and 1540 W/g (Table 1), respectively. In the case of the NC23, the temperature increase was so fast that, after 30 seconds, the AMF was switched off because the water used as solvent began to boil (Figure 2d). Seeded-growth by thermal decomposition has been reported to be a suitable method for tuning the size of magnetic nanoparticles.[18,43] However, it also provides nanoparticles with antiphase boundaries that result in lower-than-expected magnetic heating performances.[44,45] In these cases, seeded-growth routes provided single-core nanoparticles with single-crystal structures. In the case of the multicore NC56 and, particularly, NC23 samples, the SAR values are very high and comparable to the nanoflowers prepared by a polyol route.[5,6]

For the viability assays, PANC1 (pancreatic carcinoma), Mel202 (uveal melanoma), and MCF7 (breast adenocarcinoma) cancer cell lines were incubated with NC23 and NC56 at different concentrations for 24 hours. Then, cell viability reduction was studied 72 h after the treatment. The concentration at which cell toxicity is significant differs notably depending on the cell line and the nanoparticles studied. For NC56, considerable toxicity was detected in the three cell lines at concentrations higher than 0.05 mg of iron per mL (Figure 3). For NC23, significant cell toxicity appeared with concentrations higher than 0.075 mg·mL^{-1}, in PANC1 cells and Mel202 cells, and higher than 0.15 mg·mL^{-1} in MCF7 cells. Therefore, an incubation concentration of 0.05 mg·mL^{-1} was chosen for the following characterization experiments.

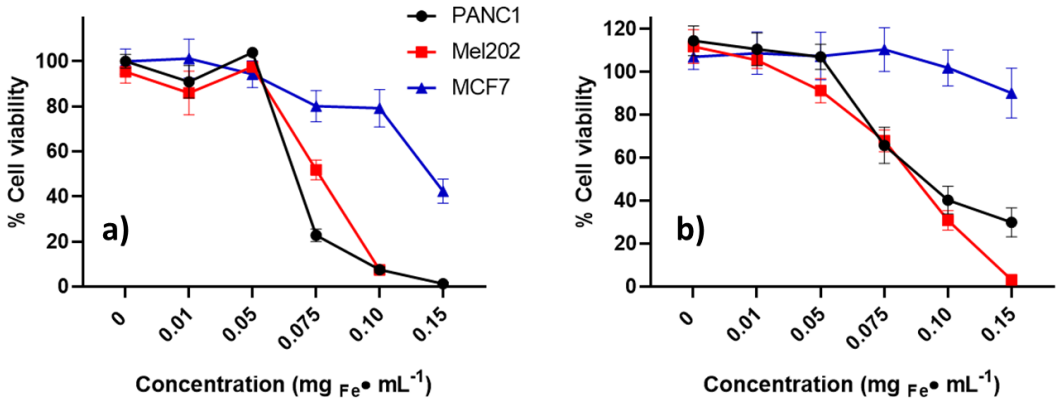

Figure 3. Cell viability studies assessed by the resazurin assay in PANC1, Mel202, and MCF7 cell lines 72h after treatment with: (a) NC23. (b) NC56.

For inducing cell death through magnetic heating, it is important that the nanoparticles are associated or attached to the cells, preferably internalized into them. Therefore, the cell internalization was evaluated by transmission electron microscopy (TEM) after 24 hours of incubation with NC23 and NC56 (Figure 4). Remarkably, TEM micrographs show that the shape and size of both NC23 and NC56 is preserved (for example, the distinctive flower-like shape of NC56 can be perfectly identified in Figure 4 d-f). The nanoparticles can be detected either close to the membrane, during the process of internalization,

suggesting an endocytosis mechanism (Figure 4 e), or into the cytoplasm. TEM micrographs mostly show the accumulation of nanoparticles inside the cytoplasm in all cell lines. Nanoparticles seem to be contained in the endosomal compartment in numbers varying from 3 to 25 nanoparticles (Figure 4d, f and l) to several dozens of nanoparticles per endosome vesicle (Figure 4j and k).

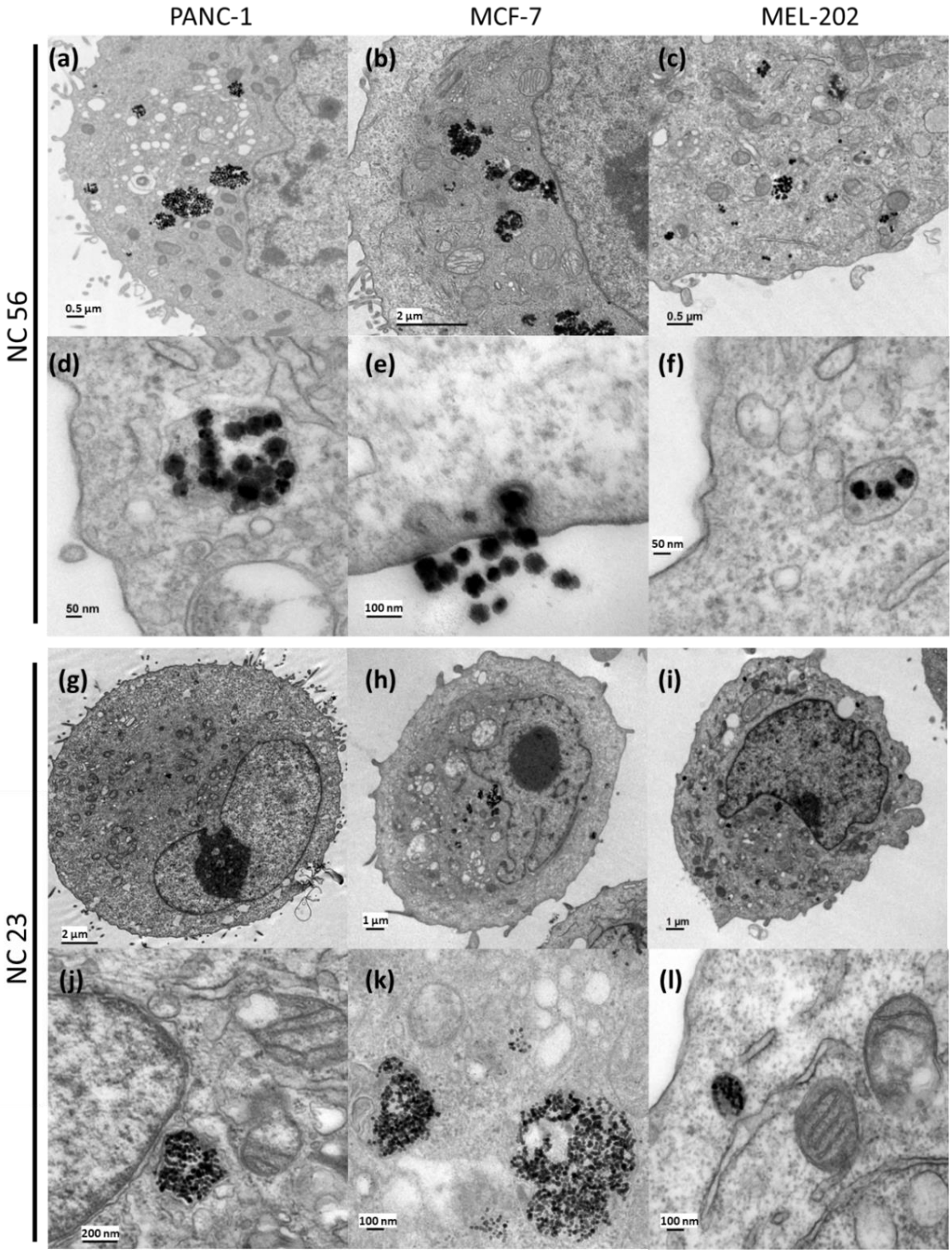

Figure 4. Selected TEM micrographs of PANC1 (a, d, g, j), MCF7 (b, e, h, k) and Mel202 (c, f, I, l) cell lines incubated with NC56 (a-f) and NC23 (g-l).

The amount of iron attached or internalized into the cells has been quantified by a colorimetric ferrozine assay for different incubation times: 2, 4, 8, 24, 48, and 72 hours. In all cases, for the two types of nanoparticles and the three cell lines, the concentration of iron detected in the cells grew continuously with the incubation time (Figure 5), which means that cells kept on internalizing nanoparticles even after 72 hours. To account for cell division, the mass of iron per cell (in pg_{Fe}/cell) has also been calculated. The concentration of iron per cell is higher with the NC56 than with the NC23 nanoparticles by 1-2 orders of magnitude (Table S2). For both nanoparticles, the internalization rate is faster within the first 8 hours of incubation. After that time the evolution of iron per cell differs depending on the type of nanoparticles and cell line. Notably, the incorporation of NC23 nanoparticles per cell does not reach a maximum in any of the cell lines studied. This is probably because of the relatively small amount of nanoparticles incorporated, with maxima of 1.05 pg_{Fe}/cell after 24 h (PANC1) and 2.24 pg_{Fe}/cell after 72 h (Mel202). In contrast, the internalization of NC56 nanoparticles does reach a maximum around 50 pg_{Fe}/cell. It seems that the cells are saturated with NC56 nanoparticles. The maximum is reached at different times that depend on the cell line: 54.2-47.7 pg_{Fe}/cell after 8-24 h (PANC1), 52.9-48.5 pg_{Fe}/cell after 48-72 h (MCF7), and 54.9-57 pg_{Fe}/cell after 8-24 hours (Mel202).

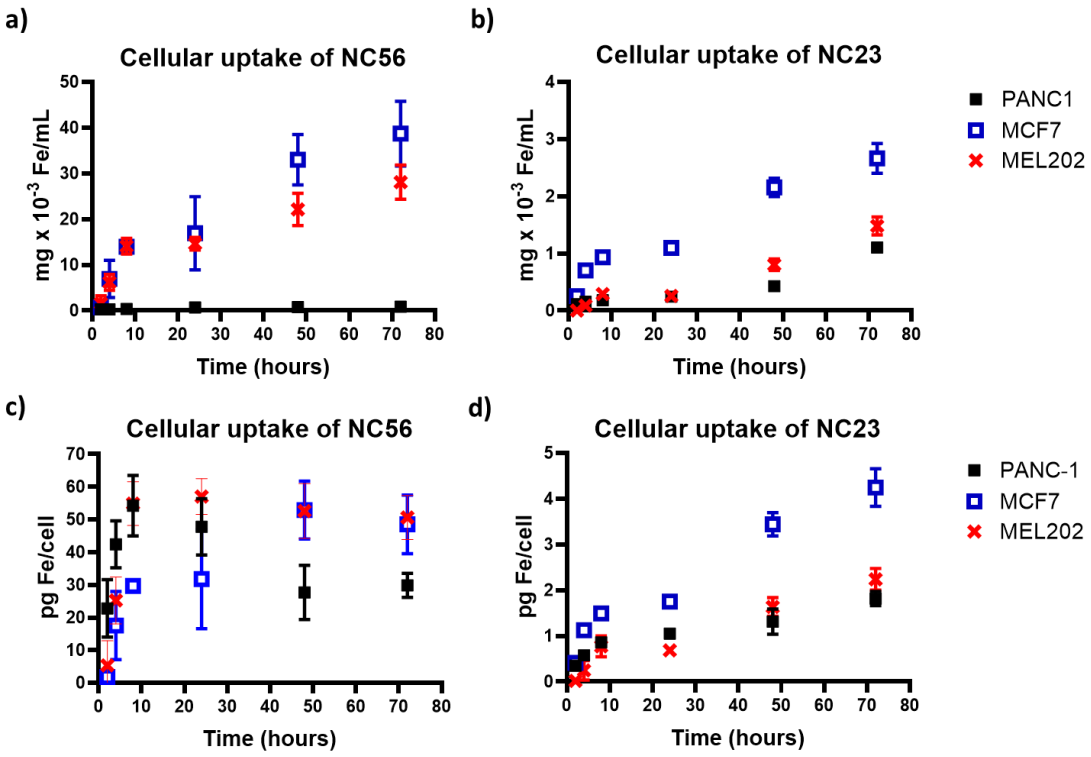

Figure 5. (a-d): Cellular uptake vs. incubation time for nanoparticles NC56 (left: a,c) and NC23 (right: b, d), measured in µg of Fe per mL (upper row: a,b) and pg of Fe per cell (lower row: c,d). The three cell lines: PANC1 (black square), MCF7 (blue hollow square) and Mel202 (red cross) were incubated with nanoparticles at an iron concentration of 0.05 $mg \cdot mL^{-1}$.

The effect of magnetic hyperthermia on cell viability was studied by comparing IONPs treatment with or without AMF. The three cell lines were incubated with NC23 or NC56 (0.05 $mg \cdot mL^{-1}$, 24 hours) and subjected to an AMF (when applicable) of 202 kHz and 23.8 $kA \cdot m^{-1}$ for 20 minutes within a thermally insulated working space at 37 ˚C. Cell viability was measured 72 hours after AMF application. When the AMF was applied, the cell viability was significantly reduced in all cell lines incubated with nanoparticles (Figure 6). The cell viability reduction was higher with NC23 than with NC56 in PANC1 (48 % and 12 %, respectively), and similar with Mel202 cells (33 % and 38 %), and MCF7 cells (14 % and 12 %). Considering the lower internalization of NC23 compared to NC56 (Figure 5, Table S2), these data imply that the efficacy of the hyperthermia treatment is greater with NC23 than with NC56

due to their larger heating ability compared to NC56 (Table 1). Indeed, although NC56 undergoes internalization to a larger extent than NC23, that difference is smaller in PANC1 cells (Figure 5, Table S2), where the magnetic hyperthermia effect on cell viability is clearly greater with NC23.

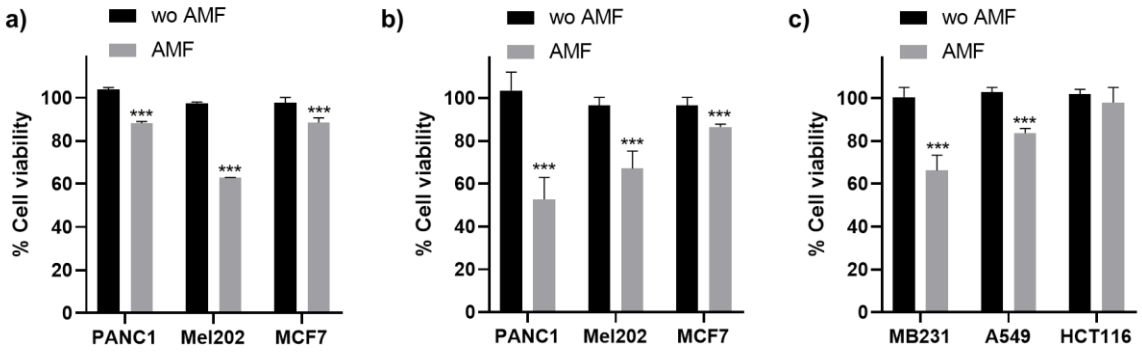

Figure 6. Results on cell viability measured by resazurin assays incubating cells for 24 h with (a) NC56 and (b-c) NC23, without applying an alternating magnetic field (AMF) and applying an AMF (202 kHz, 23.8 $kA \cdot m^{-1}$) for 20 minutes. Viabilities were measured 72 h after the AMF application. Mean values were compared against wo AMF conditions through one factor Anova *** p-value< 0.001.

Due to the heating ability and low toxicity of NC23, it was further employed in viability studies with additional cell lines (Figure 6c). Particularly in colon cancer (HCT116), lung cancer (A549), and a triple-negative breast cancer line (MB231). The approach caused a notable reduction in cell viability in MB231 cells (34 % cell viability reduction), a moderate one in A549 cells, and it was ineffective in the HCT116 cells.

To increase the efficacy of the system and search for synergies between magnetic hyperthermia, chemotherapy and gene therapy, the use of nanoparticles covalently-modified with therapeutic molecules was explored. For these studies, sample NC23 was selected due to its low toxicity and good heating properties. Regarding the therapeutic molecules, a selection of microRNAs and the chemotherapeutic drug SN38 were explored in combination with magnetic hyperthermia. Thus, two

different stock dispersions were prepared: NC23 (2 $mg_{Fe}·mL^{-1}$) functionalized with a 20 μM microRNA mixture (NC23-miRmix) and NC23 with 5 μM SN38 (NC23-SN38). The hydrodynamic size (Z-average) of these structures was 160 (PdI = 0.25) and 113 nm (PdI = 0.13), respectively, with a δ-potential of -33 mV. Using these functionalized nanostructures, protein corona studies were performed, which is relevant in the biocompatibility, biodistribution, and nanoparticle uptake.[25,46] The more abundant proteins absorbed by NC23 are transferrin, HSA, and ApOE-1, and among these, the HSA (Figure S3).

Then, the activity of the different nanostructures was evaluated through cell viability experiments in multiple cancer cell lines, including pancreatic, breast, colon, lung and melanomas (cutaneous and uveal), with and without the application of AMF (Figure 7). The data obtained shows that the activity depends on the cell line tested. The most resistant cell line to the systems and conditions used was MCF7, whose viability was reduced only when the AMF was applied. With the NC23-miRmix alone sample there is no noticeably reduction in cell viability, neither with nor without AMF (with the exception of the A549 cell line that shows a slightly lower cell viability with AMF compared with the corresponding experiment with the NC23 sample, Figure 7 d). In general, formulations that include SN38 are active with and without AMF. However, it is worth highlighting that the most active formulation implies the combination of the chemotherapeutic SN38, a mixture of therapeutic nucleic acids (miRmix) and magnetic hyperthermia (AMF). This combination presents outstanding activity in the colon cancer cell line HTC116, with a 78% of viability reduction (Figure 7 f).

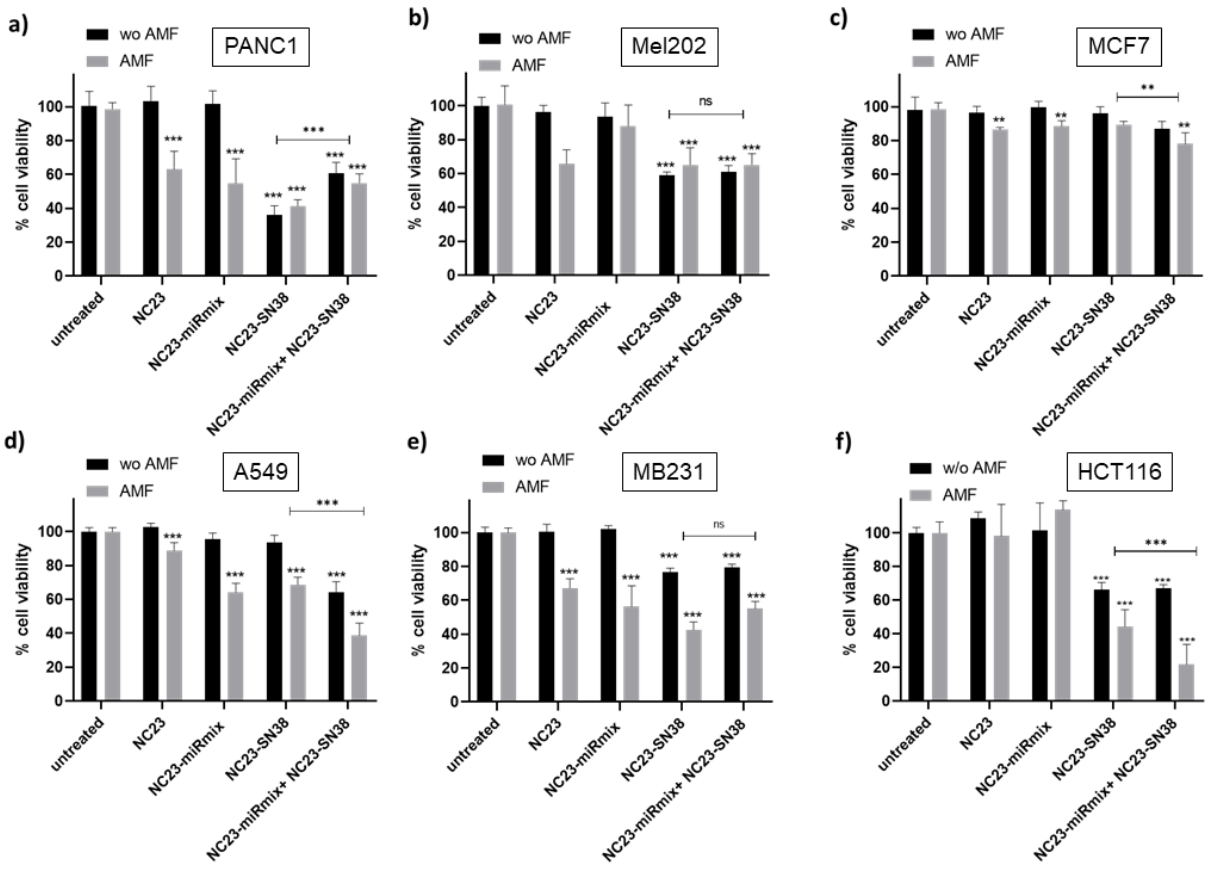

Figure 7. Results on cell viability measured by resazurin assays. Cells were treated with the different NC23 conditions for 24 h, without applying an alternating magnetic field (wo AMF) and applying an AMF (202 kHz, 23.8 $kA \cdot m^{-1}$) for 20 minutes. Viabilities were measured 72 h after the AMF application. (a) PANC1 cells. (b) Mel202 cells. (c) MCF7 cells. (d) A549. (e) MB231. (f) HCT116. NC23-miRmix concentration was 0.01 mg $_{Fe}$/mL (corresponding to miRmix 100 nM); NC23-SN38 concentration was also 0.01 mg $_{Fe}$/ mL (corresponding to SN3825 nM). The final iron concentration (0.05 mg $_{Fe}$/mL) was completed adding non-functionalized NC23 sample. Mean values were compared against wo AMF conditions through one factor Anova: *** p-value< 0.001, ** p-value<0.01, ns means non-significant.

CONCLUSIONS

It has been demonstrated that it is possible to use the thermal decomposition method to prepare multicore flower-like nanoparticles with good heating abilities under alternating magnetic fields. These nanoparticles display good colloidal stabilities, even in cell culture media. The NC56 sample is internalized by cells faster and in a larger extent than the NC23 sample. Despite its lower

internalization rate, the NC23 sample exhibits a better performance for reducing cell viabilities due to its higher heating ability. The cell viability reduction caused by magnetic hyperthermia is strongly dependent on the cell line. These results show the great antitumor potential of combination therapies, with the simultaneous addition of magnetic hyperthermia to the chemotherapeutic (SN38 drug) and gene therapy effects (microRNAs), enhancing the activity against cancer cells.

ACKNOWLEDGMENTS

This work was supported by the Ministerio de Ciencia e Innovación (PID2019-106301RB-I00 and PID2020-119352RB-I00) and Comunidad de Madrid (P2022/BMD-7403 RENIM-CM). PMR and NLG acknowledge Ministerio de Economía y Competitividad and Ministerio de Ciencia (BES-2017-082521 and FPU18/02323 fellowships). IMDEA Nanociencia acknowledges support from the 'Severo Ochoa' Programme for Centres of Excellence (Ministerio de Ciencia e Innovación, CEX2020-001039-S). Maria del Puerto Morales and Sabino Veintemillas Verdaguer (ICMM-CSIC) are gratefully acknowledged for allowing us to use their magnetic hyperthermia equipment.

SUPPLEMENTARY MATERIAL

Description: extended details on the synthesis and characterization of the nanoparticles (including iron oxide seeds of 10 nm and the derived multicore nanoparticles), oligonucleotides preparation, protein corona characterization, additional data on dynamic light scattering, and experimental values of nanoparticle internalization experiments.

REFERENCES

[1] J. Mosayebi, M. Kiyasatfar, S. Laurent, Synthesis, Functionalization, and Design of Magnetic Nanoparticles for Theranostic Applications, Adv. Healthc. Mater. 6 (2017) 1700306. https://doi.org/10.1002/adhm.201700306.

[2] H. Gavilán, S.K. Avugadda, T. Fernández-Cabada, N. Soni, M. Cassani, B.T. Mai, R. Chantrell, T. Pellegrino, Magnetic nanoparticles and clusters for magnetic hyperthermia: Optimizing their heat performance and developing combinatorial therapies to tackle cancer, Chem. Soc. Rev. 50 (2021) 11614–11667. https://doi.org/10.1039/d1cs00427a.

[3] G. Salas, S. Veintemillas-Verdaguer, M. del P. Morales, Relationship between physico-chemical properties of magnetic fluids and their heating capacity, Int. J. Hyperth. 29 (2013) 768–776. https://doi.org/10.3109/02656736.2013.826824.

[4] G. Cotin, F. Perton, C. Blanco-Andujar, B. Pichon, D. Mertz, S. Bégin-Colin, Chapter 2 - Design of Anisotropic Iron-Oxide-Based Nanoparticles for Magnetic Hyperthermia, in: R.M. Fratila, J.M.B.T.-N. for M. and O.H.A. De La Fuente (Eds.), Micro Nano Technol., Elsevier, 2019: pp. 41–60. https://doi.org/https://doi.org/10.1016/B978-0-12-813928-8.00002-8.

[5] P. Hugounenq, M. Levy, D. Alloyeau, L. Lartigue, E. Dubois, V. Cabuil, C. Ricolleau, S. Roux, C. Wilhelm, F. Gazeau, R. Bazzi, Iron Oxide Monocrystalline Nanoflowers for Highly Efficient Magnetic Hyperthermia, J. Phys. Chem. C. 116 (2012) 15702–15712. https://doi.org/10.1021/jp3025478.

[6] L. Lartigue, P. Hugounenq, D. Alloyeau, S.P. Clarke, M. Lévy, J.-C. Bacri, R. Bazzi, D.F. Brougham, C. Wilhelm, F. Gazeau, Cooperative organization in iron oxide multi-core nanoparticles potentiates their efficiency as heating mediators and MRI contrast agents., ACS Nano. 6 (2012) 10935–10949. https://doi.org/10.1021/nn304477s.

[7] D. Sakellari, K. Brintakis, A. Kostopoulou, E. Myrovali, K. Simeonidis, A. Lappas, M. Angelakeris, Ferrimagnetic nanocrystal assemblies as versatile magnetic particle hyperthermia mediators, Mater. Sci. Eng. C. 58 (2016) 187–193. https://doi.org/10.1016/j.msec.2015.08.023.

[8] G. Hemery, A.C. Keyes, E. Garaio, I. Rodrigo, J.A. Garcia, F. Plazaola, E. Garanger, O. Sandre, Tuning Sizes, Morphologies, and Magnetic Properties of Monocore Versus Multicore Iron Oxide Nanoparticles through the Controlled Addition of Water in the Polyol Synthesis, Inorg. Chem. 56 (2017) 8232–8243. https://doi.org/10.1021/acs.inorgchem.7b00956.

[9] H. Gavilán, E.H. Sánchez, M.E.F. Brollo, L. Asín, K.K. Moerner, C. Frandsen, F.J. Lázaro, C.J. Serna, S. Veintemillas-Verdaguer, M.P. Morales, L. Gutiérrez, Formation Mechanism of Maghemite Nanoflowers Synthesized by a Polyol-Mediated Process, ACS Omega. 2 (2017) 7172–7184. https://doi.org/10.1021/acsomega.7b00975.

[10] L. Storozhuk, M.O. Besenhard, S. Mourdikoudis, A.P. LaGrow, M.R. Lees, L.D. Tung, A. Gavriilidis, N.T.K. Thanh, Stable Iron Oxide Nanoflowers with Exceptional Magnetic Heating Efficiency: Simple and Fast Polyol Synthesis, ACS Appl. Mater. Interfaces. 13 (2021) 45870–45880. https://doi.org/10.1021/acsami.1c12323.

[11] E. Bertuit, E. Benassai, G. Meriguet, J.M. Greneche, B. Baptiste, S. Neveu, C. Wilhelm, A. Abou-Hassan, Structure-Property-Function Relationships of Iron Oxide Multicore Nanoflowers in Magnetic Hyperthermia and Photothermia, ACS Nano. 16 (2022) 271–284. https://doi.org/10.1021/acsnano.1c06212.

[12] O. Gerber, B.P. Pichon, C. Ulhaq, J.M. Grenèche, C. Lefevre, I. Florea, O. Ersen, D. Begin, S. Lemonnier, E. Barraud, S. Begin-Colin, Low Oxidation State and Enhanced Magnetic Properties Induced by Raspberry Shaped Nanostructures of Iron Oxide, J. Phys. Chem. C. 119 (2015) 24665–24673. https://doi.org/10.1021/acs.jpcc.5b08164.

[13] W. Cai, J. Wan, Facile synthesis of superparamagnetic magnetite nanoparticles in liquid polyols., J. Colloid Interface Sci. 305 (2007) 366–370. https://doi.org/10.1016/j.jcis.2006.10.023.

[14] A.G. Roca, L. Gutiérrez, H. Gavilán, M.E. Fortes Brollo, S. Veintemillas-Verdaguer, M. del P. Morales, Design strategies for shape-controlled magnetic iron oxide nanoparticles, Adv. Drug Deliv. Rev. 138 (2019) 68–104. https://doi.org/10.1016/j.addr.2018.12.008.

[15] Z. Xiao, Q. Zhang, X. Guo, J. Villanova, Y. Hu, I. Külaots, D. Garcia-Rojas, W. Guo, V.L. Colvin, Libraries of Uniform Magnetic Multicore Nanoparticles with Tunable Dimensions for Biomedical and Photonic Applications, ACS Appl. Mater. Interfaces. 12 (2020) 41932–41941. https://doi.org/10.1021/acsami.0c09778.

[16] R. Di Corato, A. Espinosa, L. Lartigue, M. Tharaud, S. Chat, T. Pellegrino, C. Ménager, F. Gazeau, C. Wilhelm, Magnetic hyperthermia efficiency in the cellular environment fordifferent nanoparticle designs, Biomaterials. 35 (2014) 6400–6411. https://doi.org/10.1016/j.biomaterials.2014.04.036.

[17] E.P. McKiernan, C. Moloney, T.R. Chaudhuri, S. Clerkin, K. Behan, R.M. Straubinger, J. Crean, D.F. Brougham, Formation of hydrated PEG layers on magnetic iron oxide nanoflowers shows internal magnetisation dynamics and generates high in-vivo efficacy for MRI and magnetic hyperthermia, Acta Biomater. 152 (2022) 393–405. https://doi.org/10.1016/j.actbio.2022.08.033.

[18] S. Sun, H. Zeng, Size-Controlled Synthesis of Magnetite Nanoparticles, J. Am. Chem. Soc. 124 (2002) 8204–8205. https://doi.org/10.1021/ja026501x.

[19] L. Zhang, Y.H. Dou, H.C. Gu, Sterically induced shape control of magnetite nanoparticles, J. Cryst. Growth. 296 (2006) 221–226. https://doi.org/10.1016/j.jcrysgro.2006.08.010.

[20] F. Hu, K.W. MacRenaris, E. A. Waters, E.A. Schultz-Sikma, A.L. Eckermann, T.J. Meade, Highly dispersible, superparamagnetic magnetite nanoflowers for magnetic resonance imaging, Chem.

Commun. 46 (2010) 73–75. https://doi.org/10.1039/b916562b.

[21] A.A. Nikitin, I. V. Shchetinin, N.Y. Tabachkova, M.A. Soldatov, A. V. Soldatov, N. V. Sviridenkova, E.K. Beloglazkina, A.G. Savchenko, N.D. Fedorova, M.A. Abakumov, A.G. Majouga, Synthesis of Iron Oxide Nanoclusters by Thermal Decomposition, Langmuir. 34 (2018) 4640–4650. https://doi.org/10.1021/acs.langmuir.8b00753.

[22] D. García-Soriano, P. Milán-Rois, N. Lafuente-Gómez, C. Navío, L. Gutiérrez, L. Cussó, M. Desco, D. Calle, Á. Somoza, G. Salas, Iron oxide-manganese oxide nanoparticles with tunable morphology and switchable MRI contrast mode triggered by intracellular conditions, J. Colloid Interface Sci. 613 (2022) 447–460. https://doi.org/10.1016/j.jcis.2022.01.070.

[23] C. Bidaud, D. García-Soriano, E.H. Sánchez, J.-M. Grenèche, J.A. De Toro, M. Varela, M. Dhanjani, A. Bollero, G. Salas, Tuning the exchange-coupling effect in raspberry-like γ-Fe2O3@CoO nanoparticles engineered through the single variation of the surfactant concentration in the synthesis process, Mater. Chem. Front. (2023). https://doi.org/10.1039/D2QM00834C.

[24] F.J. Slack, A.M. Chinnaiyan, The Role of Non-coding RNAs in Oncology, Cell. 179 (2019) 1033–1055. https://doi.org/10.1016/j.cell.2019.10.017.

[25] N. Lafuente-Gómez, S. Wang, F. Fontana, M. Dhanjani, D. García-Soriano, A. Correia, M. Castellanos, C. Rodriguez Diaz, G. Salas, H.A. Santos, Á. Somoza, Synergistic immunomodulatory effect in macrophages mediated by magnetic nanoparticles modified with miRNAs, Nanoscale. 14 (2022) 11129–11138. https://doi.org/10.1039/d2nr01767a.

[26] P. Milán Rois, A. Latorre, C. Rodriguez Diaz, Á. del Moral, Á. Somoza, Reprogramming Cells for Synergistic Combination Therapy with Nanotherapeutics against Uveal Melanoma, Biomimetics. 3 (2018) 28. https://doi.org/10.3390/biomimetics3040028.

[27] C.A. Schneider, W.S. Rasband, K.W. Eliceiri, NIH Image to ImageJ: 25 years of image analysis,

Nat. Methods. 9 (2012) 671–675. https://doi.org/10.1038/nmeth.2089.

[28] G. Salas, J. Camarero, D. Cabrera, H. Takacs, M. Varela, R. Ludwig, H. Dähring, I. Hilger, R. Miranda, M.D.P. Morales, F.J. Teran, Modulation of magnetic heating via dipolar magnetic interactions in monodisperse and crystalline iron oxide nanoparticles, J. Phys. Chem. C. 118 (2014) 19985–19994. https://doi.org/10.1021/jp5041234.

[29] G. Salas, C. Casado, F.J. Teran, R. Miranda, C.J. Serna, M.P. Morales, Controlled synthesis of uniform magnetite nanocrystals with high-quality properties for biomedical applications, J. Mater. Chem. 22 (2012) 21065–21075. https://doi.org/10.1039/c2jm34402e.

[30] A. Latorre, P. Couleaud, A. Aires, A.L. Cortajarena, Á. Somoza, Multifunctionalization of magnetic nanoparticles for controlled drug release: A general approach, Eur. J. Med. Chem. 82 (2014) 355–362. https://doi.org/10.1016/j.ejmech.2014.05.078.

[31] J. Riemer, H.H. Hoepken, H. Czerwinska, S.R. Robinson, R. Dringen, Colorimetric ferrozine-based assay for the quantitation of iron in cultured cells, Anal. Biochem. 331 (2004) 370–375. https://doi.org/10.1016/j.ab.2004.03.049.

[32] M. Geppert, M. Hohnholt, L. Gaetjen, I. Grunwald, M. Bäumer, R. Dringen, Accumulation of iron oxide nanoparticles by cultured brain astrocytes, J. Biomed. Nanotechnol. 5 (2009) 285–293. https://doi.org/10.1166/jbn.2009.1033.

[33] D.R. Lide, ed., Physical and Optical Properties of Minerals, in: CRC Handb. Chem. Phys., CRC Press, Boca Raton, FL, 2005: pp. 4-151-4–157. http://www.hbcpnetbase.com.

[34] G. Salas, C. Casado, F.J. Teran, R. Miranda, C.J. Serna, M.P. Morales, Controlled synthesis of uniform magnetite nanocrystals with high-quality properties for biomedical applications, J. Mater. Chem. 22 (2012) 21065–21075. https://doi.org/10.1039/C2JM34402E.

[35] R.M. Cornell, U. Schwertmann, Chapter 6. Electronic, electrical and magnetic properties and

colour, in: Iron Oxides Struct. Prop. React. Occur. Uses, 2nd ed., Wiley-VCH Verlag GmbH & Co. KGaA, Weinheim, Germany, 2003: pp. 111–137.

[36] H. Shokrollahi, A review of the magnetic properties, synthesis methods and applications of maghemite, J. Magn. Magn. Mater. 426 (2017) 74–81. https://doi.org/10.1016/j.jmmm.2016.11.033.

[37] H. Gavilán, E.H. Sánchez, M.E.F. Brollo, L. Asín, K.K. Moerner, C. Frandsen, F.J. Lázaro, C.J. Serna, S. Veintemillas-Verdaguer, M.P. Morales, L. Gutiérrez, Formation Mechanism of Maghemite Nanoflowers Synthesized by a Polyol-Mediated Process, ACS Omega. 2 (2017) 7172–7184. https://doi.org/10.1021/acsomega.7b00975.

[38] P. Bender, J. Fock, C. Frandsen, M.F. Hansen, C. Balceris, F. Ludwig, O. Posth, E. Wetterskog, L.K. Bogart, P. Southern, W. Szczerba, L. Zeng, K. Witte, C. Grüttner, F. Westphal, D. Honecker, D. González-Alonso, L. Fernández Barquín, C. Johansson, Relating Magnetic Properties and High Hyperthermia Performance of Iron Oxide Nanoflowers, J. Phys. Chem. C. 122 (2018) 3068–3077. https://doi.org/10.1021/acs.jpcc.7b11255.

[39] S. Cheong, P. Ferguson, K.W. Feindel, I.F. Hermans, P.T. Callaghan, C. Meyer, A. Slocombe, C.H. Su, F.Y. Cheng, C.S. Yeh, B. Ingham, M.F. Toney, R.D. Tilley, Simple synthesis and functionalization of iron nanoparticles for magnetic resonance imaging, Angew. Chemie - Int. Ed. 50 (2011) 4206–4209. https://doi.org/10.1002/anie.201100562.

[40] N. Lee, Y. Choi, Y. Lee, M. Park, W.K. Moon, S.H. Choi, T. Hyeon, Water-dispersible ferrimagnetic iron oxide nanocubes with extremely high r2relaxivity for highly sensitive in vivo MRI of tumors, Nano Lett. 12 (2012) 3127–3131. https://doi.org/10.1021/nl3010308.

[41] L. Gutiérrez, L. de la Cueva, M. Moros, E. Mazarío, S. de Bernardo, J.M. de la Fuente, M.P. Morales, G. Salas, Aggregation effects on the magnetic properties of iron oxide colloids,

Nanotechnology. 30 (2019) 112001. https://doi.org/10.1088/1361-6528/aafbff.

[42] B.C. Llanos, S.M. Ocampo, L. De Cueva, G.F. Calvo, J.B. Beitia, L. Pérez, G. Salas, Á. Ayuso-Sacido, Influence of Coating and Size of Magnetic Nanoparticles on Cellular Uptake for In Vitro MRI, Nanomaterials. 11 (2021) 2888. https://doi.org/10.3390/nano11112888.

[43] J. Park, E. Lee, N.-M. Hwang, M. Kang, S.C. Kim, Y. Hwang, J.-G. Park, H.-J. Noh, J.-Y. Kim, J.-H. Park, T. Hyeon, One-nanometer-scale size-controlled synthesis of monodisperse magnetic iron oxide nanoparticles., Angew. Chem. Int. Ed. Engl. 44 (2005) 2873–2877. https://doi.org/10.1002/anie.200461665.

[44] M. Levy, A. Quarta, A. Espinosa, A. Figuerola, C. Wilhelm, M. García-Hernández, A. Genovese, A. Falqui, D. Alloyeau, R. Buonsanti, P.D. Cozzoli, M.A. García, F. Gazeau, T. Pellegrino, Correlating Magneto-Structural Properties to Hyperthermia Performance of Highly Monodisperse Iron Oxide Nanoparticles Prepared by a Seeded-Growth Route, Chem. Mater. 23 (2011) 4170–4180.

[45] A. Espinosa, A. Muñoz-Noval, M. García-Hernández, A. Serrano, J. Jiménez De La Morena, A. Figuerola, A. Quarta, T. Pellegrino, C. Wilhelm, M.A. García, Magnetic properties of iron oxide nanoparticles prepared by seeded-growth route, J. Nanoparticle Res. 15 (2013) 1514. https://doi.org/10.1007/s11051-013-1514-8.

[46] M.N. Gupta, I. Roy, How Corona Formation Impacts Nanomaterials as Drug Carriers, Mol. Pharm. 17 (2020) 725–737. https://doi.org/10.1021/ACS.MOLPHARMACEUT.9B01111.